Monitoring Yearly Change Patterns of the Surface Tidal Trail (STT) in Tidal Flats
A Novel Morphological Indicator Extracted from a Near-Infrared Terrestrial Laser Scanner

Zhan, Yujian; Aarninkhof, Stefan G.J.; Wang, Zhengbing; Zhou, Yunxuan

DOI
10.2112/JCOASTRES-D-21-00093.1

Publication date
2022

Document Version
Final published version

Published in
Journal of Coastal Research

Monitoring Yearly Change Patterns of the Surface Tidal Trail (STT) in Tidal Flats: A Novel Morphological Indicator Extracted from a Near-Infrared Terrestrial Laser Scanner

Authors: Zhan, Yujian, Aarninkhof, Stefan G.J., Wang, Zhengbing, and Zhou, Yunxuan

Source: Journal of Coastal Research, 38(5) : 1011-1020

Published By: Coastal Education and Research Foundation

URL: https://doi.org/10.2112/JCOASTRES-D-21-00093.1

Journal of Coastal Research	38	5	1011–1020	Coconut Creek, Florida	September 2022

Monitoring Yearly Change Patterns of the Surface Tidal Trail (STT) in Tidal Flats: A Novel Morphological Indicator Extracted from a Near-Infrared Terrestrial Laser Scanner

Yujian Zhan[†‡], Stefan G.J. Aarninkhof[‡], Zhengbing Wang[‡], and Yunxuan Zhou[†]*

[†]State Key Laboratory of Estuarine and Coastal Research
East China Normal University
Shanghai 200062, China

[‡]Faculty of Civil Engineering and Geosciences
Delft University of Technology
Delft 2628CN, The Netherlands

www.cerf-jcr.org

www.JCRonline.org

ABSTRACT

Zhan, Y.; Aarninkhof, S.G.J.; Wang, Z., and Zhou, Y., 2022. Monitoring yearly change patterns of the surface tidal trail (STT) in tidal flats: A novel morphological indicator extracted from a near-infrared terrestrial laser scanner. *Journal of Coastal Research,* 38(5), 1011–1020. Coconut Creek (Florida), ISSN 0749-0208.

Tidal flats play an important role in the geomorphological and biological dynamics of coasts. Research on the morphological evolution of tidal flats constitutes one of the key research issues pertaining to the sustainability of coastal ecosystems and related coastal defense issues. In this work, a novel indicator, the surface tidal trail (STT), was extracted from a near infrared terrestrial laser scanner and studied. The results show that the area intensity and size of STTs decline yearly. Meanwhile, the position shift of the peak value on the STT curves presents a similar pattern of hydrodynamic force in response to the seawall, which has been studied in previous works. Although no direct correlation between the STT intensity and the deposition rate was found, the corresponding hydrodynamic force data were not available in this work. The change process of STTs still provides a possible speculation that hydrodynamic force and the softness of tidal surfaces are two main factors that form and influence STTs. For future research, establishing the direct quantitative relationships among hydrodynamic force, topography, and STTs on different temporal and spatial scales would help to better understand this novel indicator.

ADDITIONAL INDEX WORDS: *Seawall, micro topography, surface moisture, fine-scale.*

INTRODUCTION

Tidal flats are located between marine and terrestrial systems and play an important role in the geomorphological and biological dynamics of coasts. In stark contrast to sandy and rocky intertidal zones, tidal flats are much more fragile to disturbances from both natural forces and those caused by human activities. Research on the morphological evolution of tidal flats constitutes one of the key research issues pertaining to the sustainability of coastal ecosystems and related coastal defense issues (Bouma, 2014; Kirwan and Megonigal, 2013; Thiebes *et al*., 2013). The morphological equilibrium of a tidal flat responds to many drivers, such as hydrodynamic forces, external sediment supply changes, salt marsh vegetation, and anthropogenic activities (Corenblit, 2011; Friedrichs, 2011; Green and Coco, 2014; Murray *et al*., 2008). Land reclamation and coastal engineering are important forces that can significantly change tidal flats (Luan *et al*., 2018; Wu *et al*., 2011). For example, a seawall directly affects the hydrodynamic balance (Wu and Wang, 2005) and within several years can easily change the natural morphologies of tidal flats, which take decades to hundreds of years or even longer to form.

Many previous studies have examined the two-dimensional profiles of tidal flats. Their variation has been found to shape dynamic equilibria, such as the formation of concave-up and convex-up shapes (Hu *et al*., 2015), under both natural conditions and the influences of anthropogenic activities (French, 1999; Lesourd *et al*., 2001; Li *et al*., 2016). However, these works have scarcely studied the morphological evolution in plain view due to the limitations of traditional monitoring methods. As a relatively new technology, the terrestrial laser scanning (TLS) technique is able to acquire high-accuracy surface data over a large area and has been used to monitor geomorphological changes in tidal flats over the past several years (Guarnieri *et al*., 2009; Thiebes *et al*., 2013; Xie *et al*., 2017).

Unlike TLS in other bands, near-infrared TLS is extremely sensitive to water. Previous studies have researched the surface moisture in both sandy coastal zones (Jin *et al*., 2021; Nield, Wiggs, and Squirrell, 2011; Smit *et al*., 2018) and muddy tidal flats (Tan *et al*., 2020). When scanning areas with high moisture on the surface of tidal flats, a near-infrared laser signal would be absorbed or subject to complete specular reflection (Blenkinsopp *et al*., 2010; Heritage and Hetherington, 2007) to generate nonvalue areas in the acquired point cloud data. These high-moisture areas are formed by the work of tidal currents on the surface of tidal flats. By shaping the local low-lying area and the local uplift area, the moisture of the local low-lying area is relatively higher than that of the local uplift area due to the differences in evaporation rates. Therefore, a surface tidal trail (STT), as a novel morphological indicator, is shaped by tidal currents, runoffs, wind waves, and long-shore currents. Slight undulations are caused by these external forces acting on the tidal-flat surface. After the tidal current is immersed, the difference in surface moisture content makes the water content of the local recessed area higher than

DOI: 10.2112/JCOASTRES-D-21-00093.1 received 6 July 2021; accepted in revision 1 February 2022; corrected proofs received 11 March 2022.

*Corresponding author: zhouyx@sklec.ecnu.edu.cn

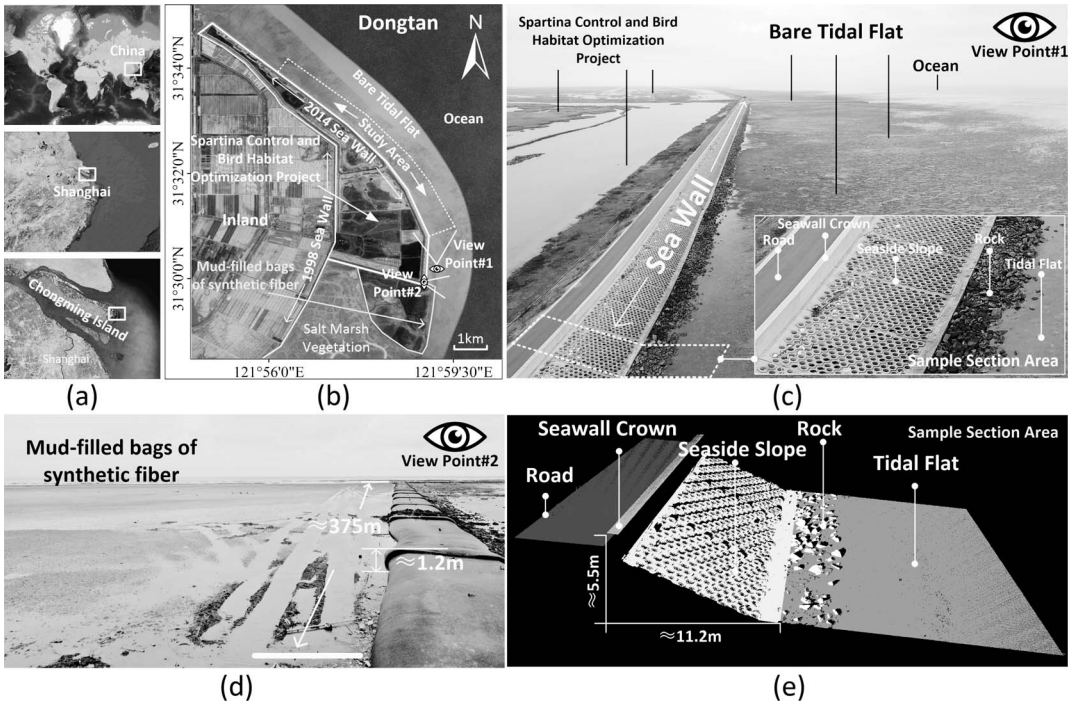

Figure 1. The location of the study area and general seawall information. (a) The location of Dongtan. (b) The area of the study site. (c) One unmanned aerial vehicle (UVA) image of the study area captured 50 m from the ground in 2018 with its position and field of view marked in (b). (d) An image of mud-filled bags captured at the SE corner of the seawall with its position and field of view marked in (b). (e) Detailed information of the seawall with its position marked in (c).

that of the surrounding area, thus forming the tidal surface traces. No previous work has yet studied these STTs in tidal flats.

This work aims to study STTs as a novel indicator in tidal flats and to research their yearly change patterns. First, the method of extracting STTs is provided, with definitions of area intensity and cross intensity curve. Then, the change process of both area intensity and the cross intensity curves are presented. Meanwhile, a statistical analysis is carried out to study the change process of STT size. Finally, the potential of STTs and the possible relationship between STTs and other indicators (deposition rate and hydrodynamic force) are discussed.

METHODS

In this section, the study area characteristics are described first, followed by descriptions of data acquisition and processing. Then, the method of extracting STTs from TLS data is presented. After that, several features from quantified STTs are calculated for further research. Finally, the statistical and correlation analysis methods are designed and constructed.

Study Area

Dongtan, which is located at the eastern end of Chongming Island, is the largest muddy tidal flat in the Yangtze Estuary (Figure 1a). The tides in the Yangtze River delta are irregularly semidiurnal, with the ranges of two successive tides being unequal. In eastern Chongming, the tidal range is 2.5 m on average and ~3.5 m during spring tides; the highest astronomical tide is 5.2 m above the lowest astronomical tide, or 1 m higher than the mean spring high tide (recorded at the Sheshan Gauging Station; Chen and Yang, 1988). Nearly half of the immense amount of sediment transported by the Yangtze River is deposited within its estuary (Fan *et al*., 2004; Jiyu *et al*., 1985). As the largest zone of deposition and the largest wetland within the Yangtze River delta, Dongtan is formed by the deposition of sediment transported downstream under the influences of runoff and tide. The sediment at the study site is dominated by mud (particle size <63 μm) and very fine sand (particle sizes between 63 μm and 125 μm) (Yang and Xu, 1995). Generally, the slope of Dongtan is relatively flat, with an average slope above the –5 m isobath of 0.24% (Yang, Yao, and He, 1999).

To implement the "Spartina Control and Bird Habitat Optimization Project," a 26.9-km-long seawall (yellow solid line in Figure 1b,c) was constructed by the CMDT (Chongming Dongtan) National Nature Reserve to encompass an area of salt marsh that was predominantly covered by *Spartina alterniflora*. Figure 1e shows one sample section of this cement seawall in three-dimensional point cloud data, which consists of the road, the seawall crown, the seaside slope, and rocks for the protection on the bare tidal flats. The seaside slope and the seawall crown were completed before September 2014, and the entire seawall project was completed in 2015. Meanwhile, the area south of the seawall (Figure 1b) is reclamated by mud-filled bags of synthetic fiber (Figure 1d).

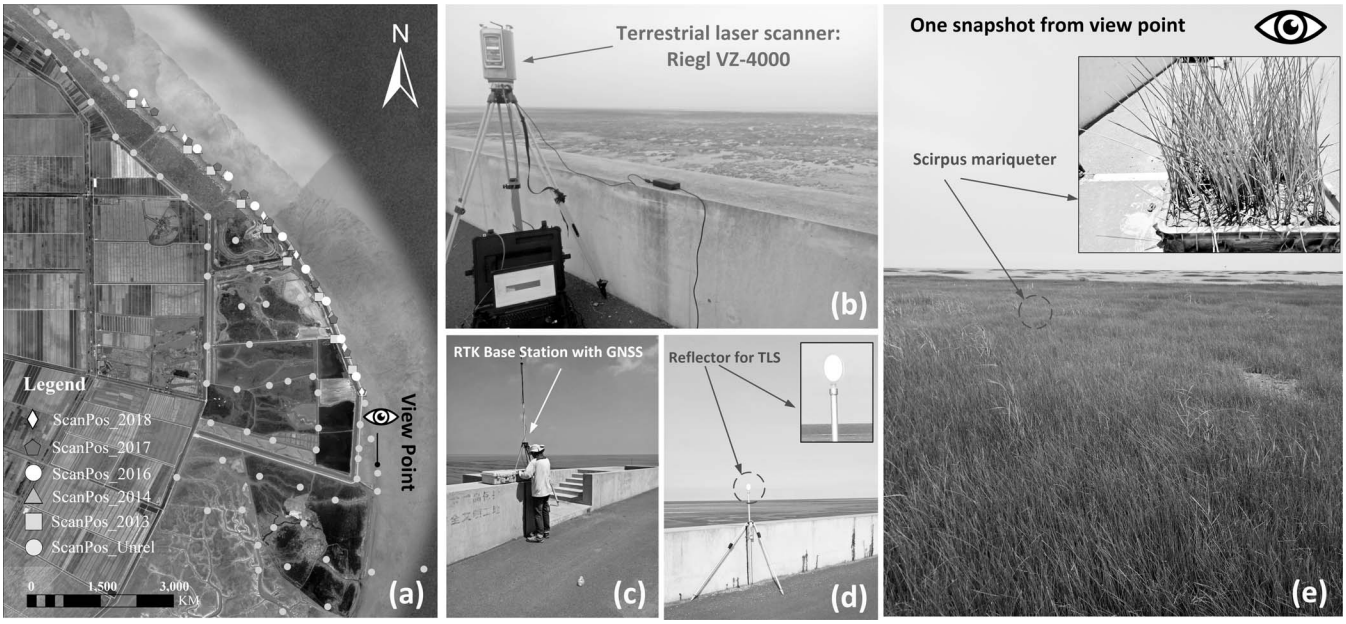

Figure 2. The scanning positions and the instruments applied in all 5 y. (a) The scanning positions. (b) The Riegl-VZ4000 in a scanning position on the seawall with a laptop generating the LIDAR data. (c) A snapshot of the real-time kinetic (RTK) base station with GNSS. (d) One reflector on the seawall, which is a flat reflector with a diameter of 5 cm. (e) A snapshot from the perspective of (b).

The study area (Figure 1b) is the bare tidal flat in front of the seawall (31°28′28″ N ~ 31°35′11″ N, 121°54′31″ ~ 122°00′22″). Its length along the seawall is nearly 8 km and 240 m in the cross-shore direction (effective range of TLS for STTs). The TLS data covered the tidal flats well before and after completion of the seawall. Thus, a suitable research environment was provided to study the yearly change pattern of the STTs.

Data Acquisition and Processing

Five field surveys were carried out from 2013 to 2018 to gather LIDAR data of Dongtan from the ground scanning positions. Figure 2a presents all the scanning positions (the gray points) in 2013, 2014, 2016, 2017, and 2018, which covered the whole area in front of the 1998 seawall (white solid line in Figure 1b). The LIDAR data (color points located on the seawall) used in this work are a subset from these five field surveys, including 14 stations in 2013, 17 stations in 2014, 17 stations in 2016, 16 stations in 2017, and 13 stations in 2018.

TLS data of these five subsets (S1, S2, S3, S4, and S5 in Table 1) were acquired using a RIEGL VZ-4000 terrestrial laser scanner with an accuracy of 15 mm. The RIEGL VZ-4000 provides high-speed, noncontact data acquisition using a narrow infrared laser beam (wavelength of 1550 nm) (Fey *et al*., 2019) and a fast scanning mechanism. A measurement range of up to 4000 m and an efficient measurement rate up to 122,000 measurements/s, with a wide field of view of 60° vertical and 360° horizontal, are also provided. The scanning frequency was 30 Hz in this work, which enables TLS to detect the maximum range of tidal flats. The real-time kinetic (RTK) data in this work include the coordinates of the top of all reflectors (Figure 2d) and the ground true points. Both base stations and receivers (Figure 2c) were used to acquire these data. The position was determined using a real-time kinematic global position system (RTK-GP, Ashtech Corp., U.S.A.) based on the local Wusong bathymetric benchmark.

The preprocessing of TLS data included preliminary georeferencing and noise point filtering, which were carried out with RiSCAN PRO software (Riegl RiSCAN PRO 2.2.1), developed by RIEGL Laser Measurement Systems GmbH. The raw TLS data (in the coordinates of the scanner), the point pairs, and the

Table 1. *The attributes of all LIDAR data.*

Survey	Period	Duration	Number of Scans	Resolution (/m^2)	Scan Radius (m)	Survey Area (ha)
S1	08–22 Sep 2013	4 d	14	0.3 to 180.8	1440 to 2877	1416
S2	25–29 Sep 2014	5 d	17	0.3 to 6400.2	2844 to 2880	1391
S3	27–31 Jul 2016 11 Oct 2016	7 d	17	0.3 to 2041	965 to 2875	1311
S4	16–19 Aug 2017 26–30 Oct 2017	9 d	16	0.3 to 1822.3	4666 to 5161	1232
S5	15–20 Nov 2018	6 d	13	0.3 to 3642.7	4650 to 5067	1161

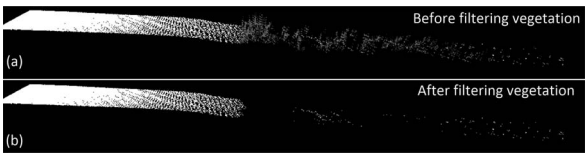

Figure 3. Salt marsh vegetation filtering, with gray points representing the salt marsh vegetation and the white points representing the tidal flats.

original transform matrixes were exported from the RiSCAN PRO software into ASCII files.

To verify the reliability of the point cloud data, a cross-section test for the overlapping area of each of the two adjacent scanning positions was carried out with two mutually perpendicular sampling lines in both the alongshore and cross-shore directions. Considering that the interval scanning time between two adjacent stations is within several hours to several days, a minimal change in tidal flats can be assumed. Thus, the curves of sample lines from any two adjacent stations should theoretically coincide with each other. Meanwhile, the root-mean-square error (RMSE) was applied to calculate the vertical error between ground RTK points and the corresponding points from the georeferenced LIDAR data.

Saltmarsh vegetation was very sparse in this study area. It was mainly distributed on the north and south sides of the study area and was filtered in the preliminary georeferenced data. Previous works provided a vegetation filtering method (Guarnieri *et al*., 2009) by using a moving window with a given search size to obtain the lowest points and consuming these points as the ground points. The vegetation in this work was low and dense, with an average height of 10 to 20 cm, and the laser may not have been able to penetrate the vegetation (Fan *et al*., 2014).

In this work, vegetation areas were first extracted by this method and then removed entirely (Figure 3). First, the TLS data resulting from each scan were clipped into several subbanded areas, with the long side oriented in the cross-shore direction. Then, the vertical thickness of each point in each subbanded area was calculated by searching its neighboring points within a given radius. Finally, these points were preliminarily classified into vegetation points and nonvegetation points based on the given threshold value of vertical thickness (5 cm in this work). After removing all the points in vegetation areas, the void areas were filled by grid points with their coordinates spatially interpolated based on nonvegetation points. All data were processed using the Point Cloud Library (Rusu and Cousins, 2011), an open-source, third-party library, and Cloud Compare software (2022), an efficient open-source tool. Considering that the vegetation area was quite small, no further discussion is presented in the Results section of this work.

STT Extraction and Change Analysis

Three main products were generated in this work. First, the STTs were extracted and quantified from the point cloud data. Then, the deposition rate was calculated. After that, the STT curves in the cross-shore direction were calculated from the quantified STTs in image space.

Table 2. *The attributes of one STT.*

Name	Description
Area	Area of the STT
Length	The minimum bidirectional rectangular length of one STT
Width	The minimum bidirectional rectangular width of one STT
Ratio	Length to width ratio

The point cloud data were first converted into Point Cloud Data (PCD) format files (a standard format supported by Cloud Compare software). Then, each PCD file was clipped based on the given rectangle (400 m in the alongshore direction and 240 m in the cross-shore direction) for further study. Next, the percentages of overlapping area between each clipped PCD were calculated. With the given threshold value, 80% in this work, the clipped PCD files were grouped to study the possible correlation between the deposition rate and cross-intensity curve.

With the clipped georeferenced PCD files, the STTs were extracted from these cloud points. The average distance (d_{avg}) of each point in the clipped PCD files with its six neighboring points was first calculated. Then, a grid (resolution of 0.1 m) was generated within the extent of each clipped PCD file. The distance ($d_{nearest}$) between each grid point and its nearest point (NP) in PCD files was calculated. Next, $d_{nearest}$ was compared to the d_{avg} of NP as mentioned above. If $d_{nearest}$ was larger than d_{avg}, the current grid point was kept as an STT point. After all STT points were extracted from the grid, these points were converted into an image space based on OpenCV Library, with one pixel representing 0.1 m. After applying the connectivity analysis algorithm and calculating the smallest circumscribed rectangle, each STT was finally quantified with its attributes, as shown in Table 2.

The area intensity value and the intensity curve in the cross-shore direction were calculated by using Equations (1) and (2) as follows:

$$Intensity_{area} = \frac{\sum_{k=0}^{n} PV_k}{n}, \quad \text{if } PV_k = 255 \tag{1}$$

$$\begin{cases} f_{crossIntensity} = f\left(Intensity_j\right) \\ Intensity_j = \frac{\sum_{i=0}^{n} PV_{ij}}{n_j}, \quad \text{if } PV_{ij} = 255 \end{cases} \tag{2}$$

where, $Intensity_{area}$ is the area intensity value of one scanning station; n is the total number of pixels; PV_k and PV_{ij} stand for the value of the current pixel; i and j are the column index (in cross-shore direction) and the row index (in alongshore direction) of the image, respectively; and n_j is the pixel number of each row.

To show the extraction effect of STTs, six subareas (Figure 4) were selected from the sample areas. A statistical analysis was completed by classifying the STTs into three types based on their widths (Table 3). Finally, one region of interest (ROI) area was selected to present the yearly change process of STTs.

Statistical Analysis

To study the possible factors in the formation of STTs, several preliminary statistical analyses were carried out. The characteristics of the intensity curve itself were first researched by

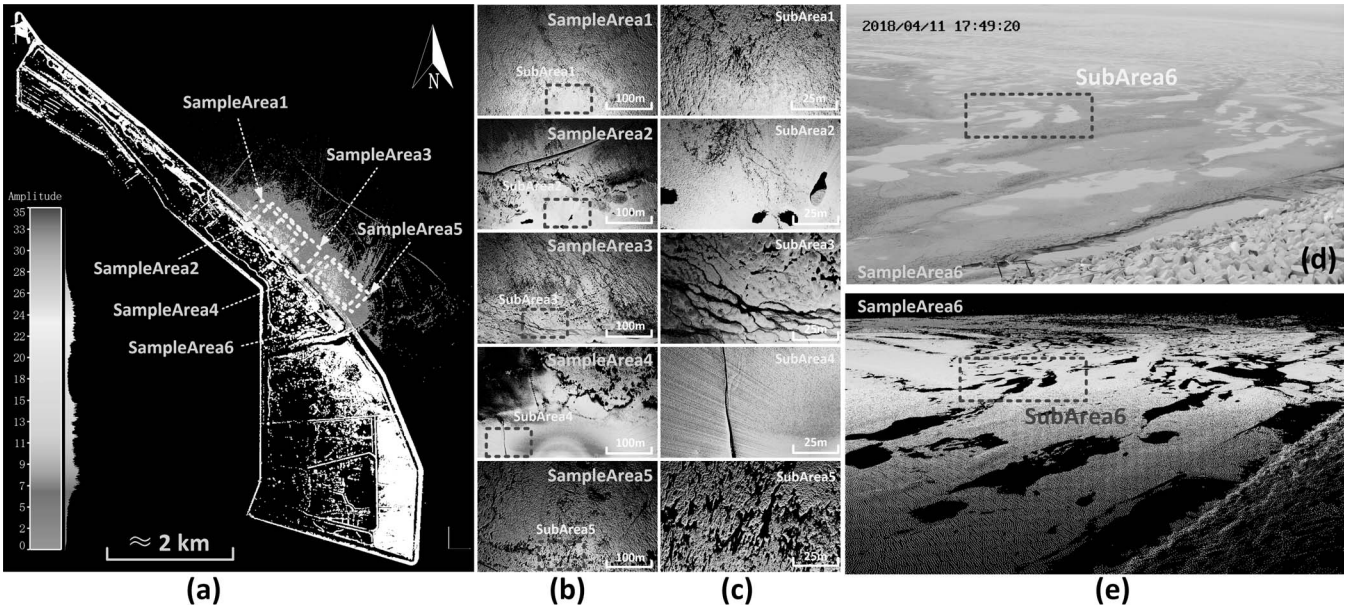

Figure 4. The locations of six sample areas for STT extraction. (a) The original point cloud of six sample areas. (b, c) The near-infrared laser signal is fully absorbed (black area), and the signaled area is observed on multiple scales. (c) A snapshot from the local Coastal Video System. (d) The point cloud data rendered from the same field of view of (c).

analyzing the correlation between intensity curves and the distance from the seawall. Then, the deposition rate was calculated to explore the correlation between it and the intensity on the STT curves.

The deposition rate curves were generated from clipped PCD files. Based on the centerlines from the position of the STT curves, the average topographic curves were first generated. Then, the deposition rate curves could be calculated by subtracting the topographic curves in two adjacent years.

The Pearson correlation coefficient (r) has been widely used to determine the strength and direction of a linear dependence between paired variables. Normally, the r value of two variables $X = (x1, x2, \ldots, xn)$ and $Y = (y1, y2, \ldots, yn)$ is defined as follows:

$$r = \frac{\sum(x_i - \bar{x})\sum(y_i - \bar{y})}{\sqrt{\sum(x_i - \bar{x})^2}\sqrt{(y_i - \bar{y})^2}} \quad r \in [-1, 1] \tag{3}$$

where, $\bar{x}$ presents the mean of X and $\bar{y}$ stands for the mean of Y. The positive sign of r illustrates that the variables are directly related, and the negative sign shows that they are inversely related. Five strength levels can be reflected according to the absolute value of r: r = [0, 0.19], very weak; r = [0.20, 0.39], weak; r = [0.40, 0.59], moderate; r = [0.60, 0.79], strong; r = [0.80, 1.0], very strong (Chen *et al.*, 2021).

Table 3. *Classification of STTs into three types based on their width.*

Type	Description
Small	The width is smaller than 2 m
Middle	The width is between 2 m and 10 m
Big	The width is bigger than 10 m

RESULTS

The LIDAR data reliability is first presented in this section. Then, the extraction result of STTs is presented. After that, the change process of STTs is studied. Finally, the correlation analysis is presented to study the possible factors that form and influence the STTs.

LIDAR Data Reliability

The improvement effects of two adjacent LIDAR data points in both the alongshore direction and cross-shore direction are presented in Figure 5a and b, respectively. All RMSEs of the sample lines are within 0.04 m in both directions.

Figure 5c shows the vertical errors between the RTK data of the ground points and the points from the TLS data. The errors in 2013 are mainly within 0.1 m, and those in other years are mainly within 0.05 m. The yearly average deposition rate is 0.157 m/a in this work, which is nearly six times that before 2013, according to previous work (Liu *et al.*, 2010). Considering this significant topographic change under the influence of the seawall, the data quality is reliable enough for this work. The possible reason why the errors in 2013 are greater than those in other years is that the scanner was set up on the surface of tidal flats, which may cause a slight posture change during the scanning process.

STT Extraction Results and Change Process

Figure 6 illustrates the extraction results of STTs from six sample areas as mentioned previously (Figure 4). The second row presents the points (blue ones) of STTs, and the first row presents those (white ones) of tidal flats. The third row shows the extraction results in the image space with the white pixels representing the STTs. The effect of extracting the results can

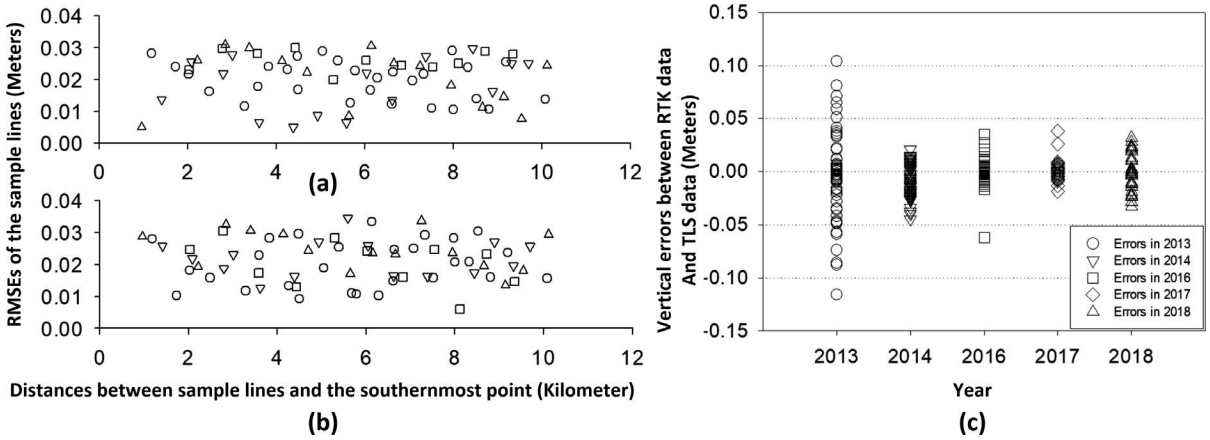

Figure 5. The data quality of LIDAR data. (a,b) The errors of all sample lines. (c) The errors between the RTK data of ground points and the points interpolated from LIDAR data.

be directly judged by visual inspection of the overlapping results in the second row, which can generally reflect the STTs. Meanwhile, by comparing the extraction results with the supervised segmentation results of subarea 6, the extraction accuracy of STT is determined as 97.48%.

The area intensity of the STTs at each scanning station is shown in Figure 7a. An overall decreasing trend (from 8.73% in 2013 to 3.06% in 2018) is observed from the average curve, with a slight increase in 2014 (8.85%) and a stabilizing trend in the last 2 years.

The cross-intensity curves within 240 m from the seawall are generated from the STT images. Figure 7b illustrates the cross-intensity spatial distribution maps by interpolating all intensity curves in all positions for each year. The red line in each map shows the position of the peak value (PPV) on each intensity curve.

Under natural conditions (in 2013), the intensity of STTs near the future seawall is stronger than those far away from the seawall. However, the intensity map in 2014 presents the opposite state. The PPVs move far away from the seawall with an average moving distance of 183 m. In 2016, after 2 years of the seawall influence, the PPVs retreat back to the seawall with an average distance of 185 m. In the last 2 years, a slight moving trend is observed, with an average moving distance of 11 m in 2017 and 4 m in 2018.

The statistical analysis of the quantified STTs is illustrated in Figure 7c. These STTs are classified into three types (small, middle, and large) according to Table 2. Each symbol point (Figure 7c) represents the area proportion of those three types of STTs in one scanning position. In 2013, the proportion points of STTs were mainly in the center triangle (50%) and the bottom left triangle (35.7% big-type points). Less than 14.3% of the points are located at the top triangle (middle-type points). In 2014, the points were concentrated on the bottom left triangle (71.4%), leaving 35.7% points in the center triangle. In 2016, 28.6% of the scanning areas were dominated by small-

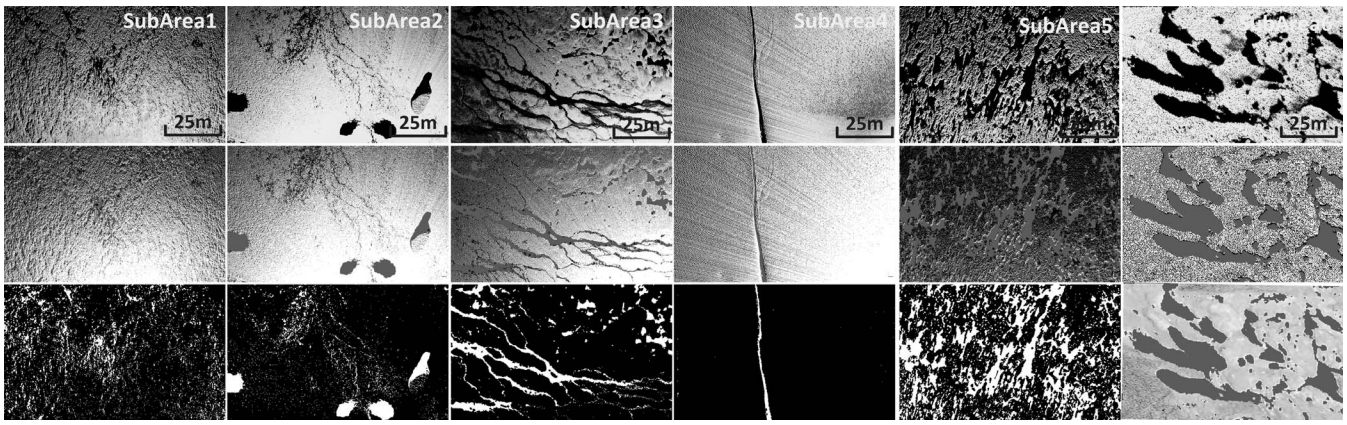

Figure 6. The original point cloud (first row), the extraction results (gray points) overlaid on the original data (white points) (second row), and the OpenCV extraction results (third row).

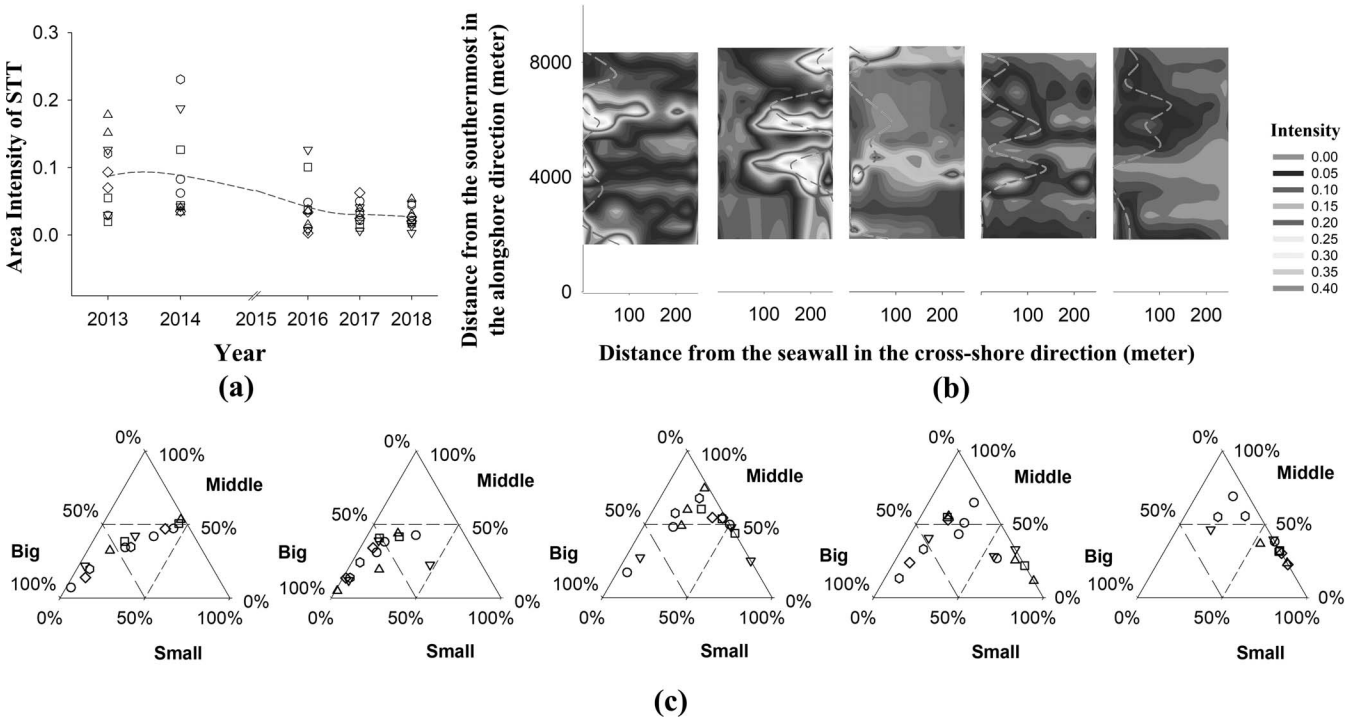

Figure 7. The whole intensity cluster, with each point representing the intensity of a single scanning station. (a) The cross-intensity contour plots and the statistical results of STTs of different sizes. (b) The x-axis (lower side) represents the area ratio within a width of 2 m, the y-axis (right side) represents the area ratio of the width of 2–10 m, and the z-axis represents the area ratio of the width of 10 m or more; 13–18 y are displayed in sequence. (c) The statistical result of the quantified STTs all five years. Each symbol point in one Ternary Plot represents the area proportion of all three types of STTs in one scanning position, with 13–18 y displayed in sequence.

type points, and 57.1% of the scanning areas were occupied by middle-type STTs, leaving only 14.3% of the points in both the bottom left triangle and the center triangle. In 2017, the percentage of small-type points increased to 42.9%. In addition, the percentage of large-type points increased slightly to 21.4%. The percentage of middle-type points dropped to 35.7%. In 2018, the small-type points (57.1%) were dominant, with 21.4% middle-type points. No large-type points were found in 2018.

ROI Change Analysis

One ROI was selected to present the STT change process. STT images, together with corresponding intensity curves, topographic profiles, and size statistics results, are studied in this section.

In the ROI, the area intensity tends to weaken yearly, as observed from images (Figure 8a–e) and cross-intensity curves (Figure 8f–j). The average value of the area intensity first slightly decreased from 9.8% (in 2013) to 9.1% (in 2014) and then declined continuously to 4.7% (in 2018). Meanwhile, the proportion of STTs of different sizes changed obviously in both the images and ternary plot (Figure 8k). In 2013 (under natural conditions), the proportion of STTs in the three types was relatively balanced (black circle in the middle area of the ternary plot). In 2014, large STTs were dominant, and few STTs were located in the area near the seawall (Figure 8b). In the following 2 years, middle-sized STTs were dominant. Subsequently, small STTs were dominant in 2018.

The cross-intensity fitting curves (the red lines) and the topography profiles (the black lines) are shown in Figure 8f–j. A concave curve of topography formed in 2014 after completion of the seawall. The PPV moves from 0 m (intensity value is 0.23) to 210 m (0.20). Meanwhile, the intensity within 70 m approaches 0. The slope of the topographical profile ranges between 1.53% and 0.59% within the same distance to the seawall. As the distance increases from 70 m to farther away, the intensity increases continuously. The slope of the corresponding profile changes slightly at first and then tends to be stable. In the following 3 years, the PPV first retreats to 82 m, then moves to 110 m and retreats slightly to 100 m. Meanwhile, the tidal flats maintain sediment vertically with no obvious shape changes in the corresponding profiles.

Correlations Analysis

To study the possible relation between the STT and other indicators (distance in the cross-shore direction and deposition rate), two correlation analyses were carried out.

The correlation analysis between the intensity on the STT curves and the corresponding distance in the cross-shore direction is shown in Figure 9a. Each STT curve is first divided into two parts (left and right) based on its PPV. A few curves with their PPVs near the seawall or too far from the seawall (smaller than 10 m or larger than 230 m in this work) were considered as one part. A total of 94.25% of the parts show a "very strong" correlation between the intensity on the curves

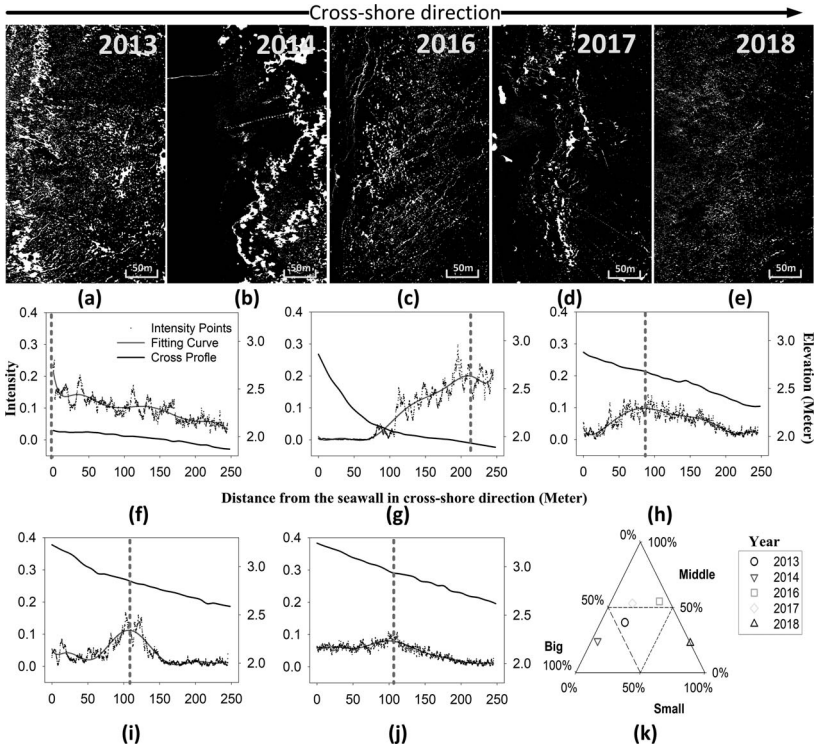

Figure 8. Trail change in ROI over 5 y. (a–e) The STTs (white pixels) in images. (f–j) The intensity on STT curves, the intensity fit curves, and the topographic profiles (black lines). (k) The proportion of STTs in different sizes.

and their distance from the seawall. The remaining parts also show a "strong" correlation, with the sig value quite close to 0.8.

The correlation between the intensity on the STT curves and the deposition rate curve was analyzed, as shown in Figure 9b. Only 15% of the values are "very strong," and 10% are "strong." Other 75% values show that the correlation is lower than "strong."

DISCUSSION

In this section, the features of STT curves are first discussed, followed by a discussion of the change pattern of STTs. Then, the possible correlation between the STT and other indicators (deposition and hydrodynamic force) is discussed. Finally, the future potential of STT is discussed.

The Feature of STT

A surface tidal trace in this work is the nondata area in the scanning zone from TLS data. Because the surface moisture or water content of an STT is higher than its local surrounding area, the near-infrared laser would be completely absorbed or specularly reflected. The shape and size of STTs are different from each other (Figure 6). As two-dimensional indicators, their sizes range from centimeters to several ten meters, with shapes varying from block to strip.

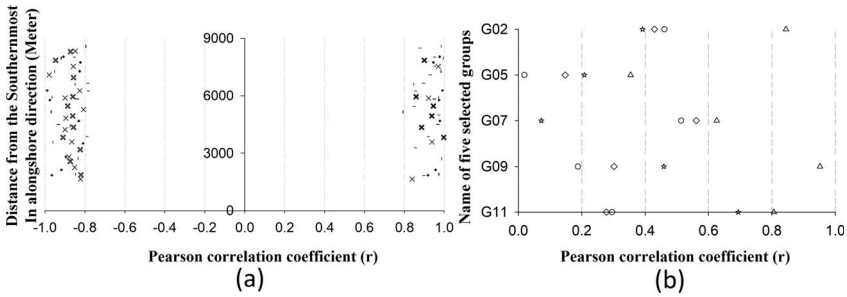

Figure 9. The value of the correlation analyses. (a) The correlation value between intensity on STTs curves and their distance from the seawall. (b) The correlation value between intensity on STTs curves and their deposition rate on topographic profiles.

A cross-intensity curve presents the spatial distribution of intensity in the cross-shore direction. Taking the intensity peak position as the dividing point, both sides of one curve show monotonicity (several intensity curves have only one side). More specifically, the left side (close to the seawall) increases monotonically, and the right side (far from the seawall) decreases monotonically.

STT Change Pattern

The area intensity declines yearly, with a slight increase in 2014. Both the curve of the area intensity (Figure 7a) and the cross-intensity spatial distribution maps (Figure 7b) illustrate a significant yearly declining trend. Meanwhile, the proportions of STTs in different sizes trend from large-size–dominated to small-size–dominated. These changes reveal two possible reasons. First, the surface of tidal flats tends to have increasing difficulty forming STTs. Second, the forces acting on the surface of tidal flats become weak.

Two correlation analyses were carried out to study the factors that cause these reasons. The intensity on the STT curves and corresponding deposition rate show no obvious relation (75% lower than strong). This analysis result reveals that the deposition rate does not directly influence the change process of STTs but should be highly correlated with the softness of the tidal surface. Meanwhile, despite the lack of hydrodynamic data in this work, it should be one of the main factors in forming STTs, which is supported by the shifting of the PPVs.

A PPV on one STT curve stands for a threshold value. This value is influenced by the softness of the tidal surface and hydrodynamic force. The position shift of the PPV illustrates the spatial changes of these two indicators in the cross-shore direction. Under natural conditions (in 2013), the PPV is concentrated near the future seawall (started and completed in 2014). The intensity curve of the STT decreases continuously in the cross-shore direction. However, the hydrodynamic force increases monotonically. One possible reason is that the surface of the tidal flat near the future seawall is softer than the area far away due to its faster deposition rate (Liu *et al*., 2010). After that, the PPV moved out far away after the seawall was completed in 2014. The hydrodynamic force weakened by the seawall should mainly contribute to this change. Previous work carried out in the tidal flats of Jiangsu Province (in SE China) found the distance effect of the seawall on the hydrodynamic force (Chen, 1991). In the cross-shore direction, the seawall significantly weakens the hydrodynamic force within a certain distance. Within this distance, the influence decreases as the distance increases. In the following years, with the continuous deposition process, the decrease in hydroperiod diminishes the influence of the seawall on the hydrodynamic force. Thus, the decreased influence of distance makes the PPVs move back near the seawall and tend to be stable in the last 2 years.

This changing pattern is illustrated more clearly in the ROI. The position shift in the peak value of the cross-intensity curves in the cross-shore direction shows a strong correlation with the distance from the seawall.

Potential and Future Study of STT

The area intensity is the ratio between the area of the STTs and that of the scanning zone. This indicator should be positively related to the softness of the tidal surface and the hydrodynamic strength. The formation of the STT is related to the softness of the tidal flat surface and the strength of the hydrodynamic force. The softness should be related to the deposition rate and the hydroperiod. The analysis carried out in this work has provided several preliminary lines of evidence.

In this work, the STTs were simply classified into three types. Meanwhile, the shape of STTs was not studied and should be further analyzed with corresponding hydrodynamic data, such as speed and direction. For further study, it is necessary to monitor detailed hydrodynamic force data to further study and analyze the formation mechanism of STTs and the corresponding mathematical model. The change process of STTs should be studied on smaller time scales to further understand the formation mechanism of STTs.

CONCLUSIONS

In this work, near-infrared TLS was applied to monitor the yearly change in STTs in a bare tidal flat. A seawall that was constructed and completed in the second year of this monitoring period offered a good opportunity to study the features and change patterns under the condition of hydrodynamic force influence.

After the extraction of STTs from TLS data, the area intensity of each scanning station, the size of each STT, the cross-shore intensity curves, and the PPVs of these curves were calculated and generated. The yearly change in area intensity and size change of STTs was first reviewed, followed by an analysis of PPV change. The results illustrate that the area intensity of STTs tends to be weakened and their sizes tend to be small. The yearly moving process of PPVs reveals the strong correlation between STTs and the hydrodynamic force in the cross-shore direction. However, in this work, no direct correlation was found between the STTs and the deposition rate or hydroperiod.

STTs have shown their potential as a novel indicator to study the intertidal zone in this work. For future research, establishing the direct quantitative relationships among hydrodynamic forces, topography, and STTs at multiple scales (*e.g*., yearly monthly or even daily) could be helpful to further understand this indicator. The preliminary analysis of STTs in this work may fill in the knowledge gaps in this field. However, more aspects of STTs should be further studied, such as the morphology of STTs. The shape of STTs from subarea-3 (Figure 6) illustrates a clear channel system on a small scale, which shows the similar morphology of the tidal creek system on a large scale. Continuously monitoring STTs may also contribute to studying the development of a tidal creek system from the very beginning.

ACKNOWLEDGMENTS

This paper is supported by the project "Coping with deltas in transition" within the Programme of Strategic Scientific Alliances between China and The Netherlands (PSA), financed by the Chinese Ministry of Science and Technology (MOST) Project no. 2016YFE0133700 and the Royal Netherlands Academy of Arts and Sciences (KNAW) Project no. PSA-SA-E-02.

LITERATURE CITED

Blenkinsopp, C.E.; Mole, M.A.; Turner, I.L., and Peirson, W.L., 2010. Measurements of the time-varying free-surface profile across the swash zone obtained using an industrial LIDAR. *Coastal Engineering*, 57(11–12), 1059–1065.

Bouma, T.J., 2014. Identifying knowledge gaps hampering application of intertidal habitats in coastal protection: Opportunities & steps to take. *Coastal Engineering*, 87, 147–157.

Chen, C., 1991. Development of depositional tidal flat in Jiangsu Province. *Oceanologia et Limnologia Sinica*, 22(4), 360–368 (in Chinese).

Chen, H.; Cui, H.; He, Z.; Lu, L., and Huang, Y., 2021. Influence of chloride deposition rate on rust layer protectiveness and corrosion severity of mild steel in tropical coastal atmosphere. *Materials Chemistry and Physics*, 259, 123971.

Chen, J.Y. and Yang, Q.I., 1988. *Report of Shanghai Coastal Comprehensive Investigation*. Shanghai, China: Shanghai Scientific and Technical Publishers, 390p.

Cloud Compare, 2022. http://www.cloudcompare.org/

Corenblit, D., 2011. Feedbacks between geomorphology and biota controlling Earth surface processes and landforms: A review of foundation concepts and current understandings. *Earth-Science Reviews*, 106(3–4), 307–331.

Fan, D.; Li, C.; Wang, D.; Ping, W., and Greb, A., 2004. Morphology and sedimentation on open-coast intertidal flats of the Changjiang Delta, China. *In:* Healy, T.R. (ed.), *Tidal Dynamics and Environment*. *Journal of Coastal Research*, Special Issue No. 43, pp. 23–35.

Fan, L.; Powrie, W.; Smethurst, J.; Atkinson, P.M., and Einstein, H., 2014. The effect of short ground vegetation on terrestrial laser scans at a local scale. *ISPRS Journal of Photogrammetry and Remote Sensing*, 95, 42–52.

Fey, C.; Schattan, P.; Helfricht, K., and Schöber, J., 2019. A compilation of multitemporal TLS snow depth distribution maps at the Weisssee snow research site (Kaunertal, Austria). *Water Resources Research*, 55(6), 5154–5164.

French, P.W., 1999. Managed retreat: A natural analogue from the Medway estuary, UK. *Ocean & Coastal Management*, 42(1), 49–62.

Friedrichs, C.T., 2011. Tidal flat morphodynamics: A synthesis. *In:* Flemming, B.W. and Hansom, J.D. (eds.), *Treatise on Estuarine and Coastal Science: Sedimentology and Geology*. Amsterdam: Elsevier, pp. 137–170.

Green, M.O. and Coco, G., 2014. Review of wave-driven sediment resuspension and transport in estuaries. *Reviews of Geophysics*, 52(1), 77–117.

Guarnieri, A.; Vettore, A.; Pirotti, F.; Menenti, M., and Marani, M., 2009. Retrieval of small-relief marsh morphology from Terrestrial Laser Scanner, optimal spatial filtering, and laser return intensity. *Geomorphology*, 113(1–2), 12–20.

Heritage, G. and Hetherington, D., 2007. Towards a protocol for laser scanning in fluvial geomorphology. *Earth Surface Processes and Landforms: The Journal of the British Geomorphological Research Group*, 32(1), 66–74.

Hu, Z.; Wang, Z.B.; Zitman, T.J.; Stive, M.J., and Bouma, T.J., 2015. Predicting long-term and short-term tidal flat morphodynamics using a dynamic equilibrium theory. *Journal of Geophysical Research: Earth Surface*, 120(9), 1803–1823.

Jin, J.; Verbeurgt, J.; Sloover, L.D.; Stal, C.; Deruyter, G.; Montreuil, A.L.; Vos, S.; Maeyer, P.D., and Wulfa, A.D., 2021. Monitoring spatiotemporal variation in beach surface moisture using a long-range terrestrial laser scanner. *ISPRS Journal of Photogrammetry and Remote Sensing*, 173, 195–208.

Jiyu, C.; Huifang, Z.; Yongfa, D., and Jieming, S., 1985. Development of the Changjiang estuary and its submerged delta. *Continental Shelf Research*, 4(1–2), 47–56.

Kirwan, M.L. and Megonigal, J.P., 2013. Tidal wetland stability in the face of human impacts and sea-level rise. *Nature*, 504(7478), 53–60.

Lesourd, S.; Lesueur, P.; Brun-Cottan, J.C.; Auffret, J.P.; Poupinet, N., and Laignel, B., 2001. Morphosedimentary evolution of the macrotidal seine estuary subjected to human impact. *Estuaries*, 24(6), 940–949.

Li, M.L.; Yang, L.; Gong, X.L.; Xue, W.Y.; Yang, Y.; Shi, Y., and Wang, Y.P., 2016. The geomorphologic response of accreting intertidal flat to reclamation: A case from Jianggang, Jiangsu. *Marine Science Bulletin*, 35(6), 683–693.

Liu, X.; Yang, L.J.; JunJie, X.U.; Chen, Y., and Yun, C.X., 2010. The evolution of the north branch of Yangtze River estuary characterized by being narrower and shallower. *Shanghai Geology*, 31, 35–70 (in Chinese).

Luan, H.L.; Ding, P.X.; Wang, Z.B.; Yang, S.L., and Lu, J.Y., 2018. Morphodynamic impacts of large-scale engineering projects in the Yangtze River delta. *Coastal Engineering*, 141, 1–11.

Murray, A.B.; Knaapen, M.; Tal, M., and Kirwan, M.L., 2008. Biomorphodynamics: Physical-biological feedbacks that shape landscapes. *Water Resources Research*, 44(11), 1–18.

Nield, J.M.; Wiggs, G.F., and Squirrell, R.S., 2011. Aeolian sand strip mobility and protodune development on a drying beach: Examining surface moisture and surface roughness patterns measured by terrestrial laser scanning. *Earth Surface Processes and Landforms*, 36(4), 513–522.

Rusu, R.B. and Cousins, S., 2011. 3D is here: Point cloud library (PCL). *Proceedings of the 2011 IEEE international conference on robotics and automation* (Shanghai, China), pp. 1–4.

Smit, Y.; Ruessink, G.; Brakenhoff, L.B., and Donker, J.J., 2018. Measuring spatial and temporal variation in surface moisture on a coastal beach with a near-infrared terrestrial laser scanner. *Aeolian Research*, 31(Part A), 19–27.

Tan, K.; Chen, J.; Zhang, W.; Liu, K., and Cheng, X., 2020. Estimation of soil surface water contents for intertidal mudflats using a near-infrared long-range terrestrial laser scanner. *ISPRS Journal of Photogrammetry and Remote Sensing*, 159, 129–139.

Thiebes, B.; Wang, J.; Bai, S., and Li, J., 2013. Terrestrial laser scanning of tidal flats—A case study in Jiangsu Province, China. *Journal of Coastal Conservation*, 17(4), 813–823.

Wu, C.; Cai, F.; Zhao, G.; Zheng, Y., and Lu, H., 2011. Impact of coastal engineering constructions on the topographic and morphological evolution of Quanzhou Bay, Fujian, China. *Ocean & Coastal Management*, 54(7), 544–555.

Wu, X. and Wang, A., 2005. Impacts of human beings' activities on north Jiangsu tidal flat. *Scientia Geographica Sinica*, 25(5), 614.

Xie, W.; He, Q.; Zhang, K.; Guo, L.; Wang, X., and Shen, J., 2017. Application of terrestrial laser scanner on tidal flat morphology at a typhoon event timescale. *Geomorphology*, 292, 47–58.

Yang, S. and Xu, H., 1995. Tidal flat sediments and sedimentation on the Changxin and Hengsa Islands at the mouth of Changjiang River. *Oceanographic Literature Review*, 6(42), 450–451 (in Chinese).

Yang, S.L.; Yao, Y.M., and He, S.L., 1999. Coastal profile shape and erosion–accretion changes of the sediment islands in the Changjiang River estuary. *Oceanologia et Limnologia Sinica Sin*, 30(6), 764–769 (in Chinese).